

Numerical study of the coupling layer between transducer and chip in acoustofluidic devices

William Naundrup Bodé^{1, a)} and Henrik Bruus^{1, b)}

*Department of Physics, Technical University of Denmark,
DTU Physics Building 309, DK-2800 Kongens Lyngby, Denmark*

(Dated: 28 January 2021)

We study by numerical simulation in two and three dimensions the coupling layer between the transducer and the microfluidic chip in ultrasound acoustofluidic devices. The model includes the transducer with electrodes, the microfluidic chip with a liquid-filled microchannel, and the coupling layer between the transducer and the chip. We consider two commonly used coupling materials, solid epoxy glue and viscous glycerol, as well as two commonly used device types, glass capillary tubes and silicon-glass chips. We study how acoustic resonances in ideal devices without a coupling layer is either sustained or attenuated as a coupling layer of increasing thickness is inserted. We establish a simple criterion based on the phase of the acoustic wave for whether a given zero-layer resonance is sustained or attenuated by the addition of a coupling layer. Finally, we show that by controlling the thickness and the material, the coupling layer can be used as a design component for optimal and robust acoustofluidic resonances.

©2021 Acoustical Society of America. [[http://dx.doi.org\(DOI number\)](http://dx.doi.org(DOI number))]

[XYZ]

Pages: 1–10

I. INTRODUCTION

The acoustic impedance matching techniques for piezoelectric sensors and transducers is in general a well-studied field, as exemplified by the recent review by Rathod.¹ However, specifically for ultrasound acoustofluidic devices, the role of the coupling layer (also known as the carrier or matching layer) between the transducer and the microfluidic chip remains poorly understood beyond one-dimensional (1D) planar systems.^{2,3} Whereas the function of a matching layer for 1D traveling waves through layered structures, is simply to couple acoustic energy more efficiently into subsequent layers, its role in resonant 1D acoustofluidic systems is less straightforward. As analyzed by Glynne-Jones, Boltryk, and Hill,³ the function of the coupling layer may be more structural, or to isolate the transducer from the fluid layer. In the present work, we study the more complex case of a fully three-dimensional (3D) acoustofluidic system.

We present 3D numerical simulations of a piezoelectric transducer coupled to an acoustofluidic chip through a thin coupling layer consisting of either a solid glue or a viscous liquid. We consider two commonly used types of acoustofluidic devices sketched in Fig. 1, glass capillary tubes and silicon-glass chips. Capillary-tube devices have been applied as acoustic particle traps relying on a small transducer that actuates a vertical resonant pressure mode locally in the capillary.^{4–7} Silicon-

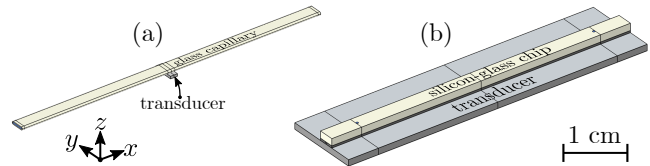


FIG. 1. Sketch of the two types of acoustofluidic devices considered in this study. (a) A glass capillary (beige) mounted on a small piezoelectric transducer (gray). (b) A silicon-glass chip (black base, beige lid) mounted on a bulk piezoelectric transducer (gray). Both sketches are drawn to scale.

glass devices have been applied for continuous-flow focusing and separation of particle suspensions relying on bulk actuation of horizontal resonance modes in embedded microchannels.^{8–10}

The paper is organized as follows: In Section II, we present the basic theory, including governing equations and boundary conditions. In Section III we model the capillary-tube particle traps and show their dependency on the coupling-layer thickness. In Section IV a similar analysis is carried out for the conventional acoustophoresis silicon-glass devices. Finally in Section V, we present a concluding discussion regarding the criterion established in the two previous sections for designing acoustofluidic devices, with acoustic resonance modes that are relatively insensitive to the thickness of the coupling layer.

a) winabo@dtu.dk

b) bruus@fysik.dtu.dk

II. THEORY AND MODEL ASSUMPTIONS

In establishing the numerical model, we follow closely the theory presented by Skov *et al.*¹¹ Our model consists of a lead-zirconate-titanate (PZT) piezoelectric transducer coupled to an elastic solid, which contains the fluid-filled microchannel. Theoretically, the system is described by three continuous fields: the electric potential φ in the PZT transducer, the mechanical displacement field \mathbf{u} in the elastic solid and the PZT transducer, and the acoustic pressure p_1 in the fluid. The coupling layer is described by p_1 if it is a liquid, and by \mathbf{u} if it is a solid. Due to the linearity of the governing equations, all fields has a harmonic time dependence $e^{-i\omega t}$ with angular frequency $\omega = 2\pi f$ and frequency f . Thus, a given field has the structure $\hat{f}(\mathbf{r}, t) = f(\mathbf{r}) e^{-i\omega t}$, and we need only determine the complex-valued space-dependent amplitude $f(\mathbf{r})$.

The acoustic pressure field p_1 is modeled using the effective pressure acoustic theory by Bach and Bruus,¹² where the viscous boundary layers are included analytically in the effective boundary conditions. Using the effective theory, the acoustic pressure p_1 in a fluid with density ρ_0 , sound speed c_0 , dynamic viscosity η_0 and bulk viscosity η^b is governed by the Helmholtz equation, and the acoustic velocity \mathbf{v}_1 is proportional to ∇p_1 ,

$$\nabla^2 p_1 = -k_c^2 p_1, \quad \mathbf{v}_1 = -i \frac{1 - i\Gamma}{\omega \rho_0} \nabla p_1, \quad (1a)$$

$$\text{with } k_0 = \frac{\omega}{c_0}, \quad k_c = \left(1 + \frac{i}{2}\Gamma\right) k_0, \quad (1b)$$

$$\text{and } \Gamma = \left(\frac{\eta^b}{\eta_0} + \frac{4}{3}\right) \frac{\omega \eta_0}{\rho_0 c_0^2}. \quad (1c)$$

In cases where the fluid coupling layer thickness Δ is comparable or smaller than the viscous boundary-layer length scale $\delta_{\text{visc}} = \sqrt{2\eta_0/(\rho_0\omega)}$, the effective theory fails, and the full perturbation model is used instead.^{13,14}

The mechanical displacement field \mathbf{u} is governed by the linear Cauchy equation involving the stress tensor $\boldsymbol{\sigma}$,

$$-\rho_0 \omega^2 \mathbf{u} = \nabla \cdot \boldsymbol{\sigma}, \quad (2)$$

The components σ_{ik} are related to the strain components $\frac{1}{2}(\partial_i u_k + \partial_k u_i)$ by the stiffness tensor \mathbf{C} , which for linear isotropic or cubic-symmetric elastic materials are written in the Voigt notation as

$$\begin{pmatrix} \sigma_{xx} \\ \sigma_{yy} \\ \sigma_{zz} \\ \sigma_{yz} \\ \sigma_{xz} \\ \sigma_{xy} \end{pmatrix} = \begin{pmatrix} C_{11} & C_{12} & C_{12} & 0 & 0 & 0 \\ C_{12} & C_{11} & C_{12} & 0 & 0 & 0 \\ C_{12} & C_{12} & C_{11} & 0 & 0 & 0 \\ 0 & 0 & 0 & C_{44} & 0 & 0 \\ 0 & 0 & 0 & 0 & C_{44} & 0 \\ 0 & 0 & 0 & 0 & 0 & C_{44} \end{pmatrix} \begin{pmatrix} \partial_x u_x \\ \partial_y u_y \\ \partial_z u_z \\ \partial_y u_z + \partial_z u_y \\ \partial_x u_z + \partial_z u_x \\ \partial_x u_y + \partial_y u_x \end{pmatrix}. \quad (3)$$

Mechanical damping is implemented as complex-valued elastic moduli, defined as $C_{ik} = (1 - i\Gamma_{\text{sl}})c_{ik}$. In the PZT transducer, the electric potential φ is governed by the quasi-static Gauss equation involving the electric dis-

placement \mathbf{D} ,

$$\nabla \cdot \mathbf{D} = 0. \quad (4)$$

Furthermore in PZT, the complete linear electromechanical coupling relating the stress and the electric displacement to the strain and the electric field is given by the Voigt notation as,

$$\begin{pmatrix} \sigma_{xx} \\ \sigma_{yy} \\ \sigma_{zz} \\ \sigma_{yz} \\ \sigma_{xz} \\ \sigma_{xy} \\ D_x \\ D_y \\ D_z \end{pmatrix} = \begin{pmatrix} C_{11} & C_{12} & C_{13} & 0 & 0 & 0 & 0 & 0 & -e_{31} \\ C_{12} & C_{11} & C_{13} & 0 & 0 & 0 & 0 & 0 & -e_{31} \\ C_{13} & C_{13} & C_{33} & 0 & 0 & 0 & 0 & 0 & -e_{33} \\ 0 & 0 & 0 & C_{44} & 0 & 0 & 0 & -e_{15} & 0 \\ 0 & 0 & 0 & 0 & C_{44} & 0 & -e_{15} & 0 & 0 \\ 0 & 0 & 0 & 0 & 0 & C_{66} & 0 & 0 & 0 \\ 0 & 0 & 0 & 0 & e_{15} & 0 & \epsilon_{11} & 0 & 0 \\ 0 & 0 & 0 & e_{15} & 0 & 0 & 0 & \epsilon_{11} & 0 \\ e_{31} & e_{31} & e_{33} & 0 & 0 & 0 & 0 & 0 & \epsilon_{33} \end{pmatrix} \begin{pmatrix} \partial_x u_x \\ \partial_y u_y \\ \partial_z u_z \\ \partial_y u_z + \partial_z u_y \\ \partial_x u_z + \partial_z u_x \\ \partial_x u_y + \partial_y u_x \\ -\partial_x \varphi \\ -\partial_y \varphi \\ -\partial_z \varphi \end{pmatrix}. \quad (5)$$

A. Acoustic energy density

Throughout this study, the time- and volume-averaged acoustic energy density E_{ac} in the water-filled channel is used as a measure and indicator of how the acoustic resonances are affected by the coupling layer. In a fluid volume V the averaged acoustic energy density is given as

$$E_{\text{ac}} = \frac{1}{V} \int \left(\frac{1}{4} \rho_0 |\mathbf{v}_1|^2 + \frac{1}{4} \kappa_0 |p_1|^2 \right) dV. \quad (6)$$

B. Boundary conditions

At the fluid-solid interface the boundary conditions are no-slip and continuous stress, together with zero stress on free surfaces. Introducing the mechanical displacement velocity $\mathbf{v}_{\text{sl}} = -i\omega \mathbf{u}$ and a shear wave number $k_s = (1 + i)/\delta_{\text{visc}}$ the effective continuous velocity and stress boundary conditions become,¹²

$$\mathbf{n} \cdot \mathbf{v}_1 = \mathbf{n} \cdot \mathbf{v}_{\text{sl}} + \frac{i}{k_s} \nabla_{\parallel} \cdot (\mathbf{v}_{\text{sl}} - \mathbf{v}_1), \quad (7a)$$

$$\boldsymbol{\sigma} \cdot \mathbf{n} = -p_1 \mathbf{n} + ik_s \eta_0 \left(\mathbf{v}_{\text{sl}} + \frac{i}{\omega \rho_0} \nabla p_1 \right), \quad (7b)$$

where the unit vector \mathbf{n} is the outward surface normal from the solid domain. In experiments, the electrical signal is driven by a sine-wave function generator coupled to the transducer electrodes, this is implemented as a constant potential boundary condition on the electrode-transducer interface. Furthermore we assume no free charges, implemented as a zero flux condition on the electric displacement field. In the 3D capillary-tube device, symmetries are exploited such that the full system can be reduced to one quarter. The boundary conditions are listed in Table I. Except for the symmetry conditions, the same boundary conditions applies for the silicon-glass device.

C. Unbounded perfectly matched layers

For long systems like the capillary tubes, a no-reflection boundary condition can be established closer to

TABLE I. List of boundary conditions used in the modeled acoustofluidic systems. The unit vector \mathbf{n} is the surface outward normal with respect to the solid domain, and \mathbf{t} is any of the two tangential unit vectors.

Domain \leftarrow boundary	Boundary condition
Solid domain \leftarrow air	$\boldsymbol{\sigma} \cdot \mathbf{n} = \mathbf{0}$
Fluid domain \leftarrow solid	Eq. (7a)
Solid domain \leftarrow fluid	Eq. (7b)
Fluid domain \leftarrow air	$p_1 = 0$
PZT domain \leftarrow bottom electrode	$\varphi = 0$
PZT domain \leftarrow top electrode	$\varphi = V_0$
Solid domain \leftarrow symmetry	$\mathbf{u} \cdot \mathbf{n} = 0, \mathbf{t} \cdot \boldsymbol{\sigma} \cdot \mathbf{n} = 0$
Fluid domain \leftarrow symmetry	$\mathbf{n} \cdot \nabla p_1 = 0$

the origin of the domain by using the perfectly matched layer (PML) technique, thus reducing the computational domain substantially. It involves a complex coordinate transformation of the form $x \rightarrow x + \frac{i}{\omega} \int^x \theta(x') dx'$, such that outgoing waves are attenuated within a distance comparable to the wavelength. The PML technique requires a choice of damping function θ , the specific function is adopted from Bermúdez *et al.*¹⁵,

$$\theta(x) = \begin{cases} 0, & \text{for } x \leq L_{\text{cap}}, \\ \frac{\beta}{L_{\text{pml}} - (x - L_{\text{cap}})} - \frac{\beta}{L_{\text{pml}}}, & \text{for } x > L_{\text{cap}}. \end{cases} \quad (8)$$

The parameters defining $\theta(x)$ is chosen appropriately for a given system: L_{cap} is the position of the interface between the physical capillary tube and the PML domain, L_{pml} is the length of the PML domain, and β is the damping strength. The axial coordinate x is complex-valued for $x > L_{\text{cap}}$ inside the PML domain. The function θ is classified as a continuous unbounded damping function, effective in terms of numerical error and reflections at the PML interface $x = L_{\text{cap}}$.¹⁵

D. Numerical implementation in COMSOL Multiphysics

The numerical model was implemented in the finite element software COMSOL Multiphysics¹⁶ using "Weak Form PDE" in the Mathematics module and closely following Ref. 11, where further implementation details can be found. The mesh settings is adopted from Ley and Bruus.¹⁷ The scripts were computed on a workstation with a 12 core 3.5 GHz CPU processor, and 128 GB ram.

III. CAPILLARY-TUBE PARTICLE TRAPS

As the first example, we investigate the capillary-tube device widely used as a versatile acoustic trap in many experimental studies.⁴⁻⁷ The corresponding model system is sketched in Fig. 2 indicating the different domains together with the PML layer and a zoom-in on the

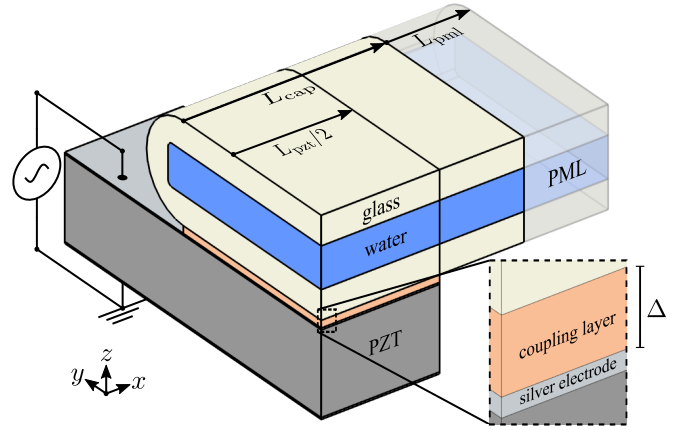


FIG. 2. One quarter of the capillary-tube-based model system with a zoom-in on the coupling layer of thickness Δ . The model system includes a water-filled glass capillary coupled to a PZT transducer with silver electrodes. The top electrode is coupled to a time-harmonic function generator and the bottom electrode is grounded.

TABLE II. The length (L), width (W), and height (H) of the glass capillary tube (cap), the channel (ch), the piezoelectric transducer (pzt), and the silver electrodes (el). The curvature of the outer and inner rounded corners are $240 \mu\text{m}$ and $25 \mu\text{m}$, respectively. The bottom $H_{\text{gl,bot}}$ and top $H_{\text{gl,top}}$ glass-wall thicknesses are both $140 \mu\text{m}$.

Symbol	Value	Symbol	Value
L_{cap}	$1573 \mu\text{m}$	L_{ch}	$1573 \mu\text{m}$
W_{cap}	$2280 \mu\text{m}$	W_{ch}	$2000 \mu\text{m}$
H_{cap}	$480 \mu\text{m}$	H_{ch}	$200 \mu\text{m}$
L_{pzt}	$1160 \mu\text{m}$	L_{el}	$1160 \mu\text{m}$
W_{pzt}	$3350 \mu\text{m}$	W_{el}	$3350 \mu\text{m}$
H_{pzt}	$400 \mu\text{m}$	H_{el}	$9 \mu\text{m}$

coupling layer. The dimensions and materials used in the numerical model are listed in Tables II and III, respectively. The model system is similar to the one studied by Ley and Bruus,¹⁷ but now the model is extended to include a PZT transducer and a coupling layer. Typically the capillary-tube device is characterized by having a standing half-wave-like resonance in the vertical direction. This is achieved with a PZT transducer having a pre-designed mode at 5 MHz, also used in preliminary experiments by the Laurell group at Lund University.

A. The specific perfectly matched layer

We implement no-reflection boundary conditions using a PML layer with parameter values $\beta = 2c_{\text{lo}}^{(\text{gl})} = 11.294 \text{ m/s}$ and $L_{\text{pml}} = 413 \mu\text{m}$. The superscript refer

TABLE III. List of parameters used in the numerical simulations. Note that $C_{12} = C_{11} - 2C_{44}$ for isotropic materials. Isotropy in the xy -plane implies $C_{66} = \frac{1}{2}(C_{11} - C_{12})$ for the PZT.

Parameter	Symbol	Value	Unit
<i>Water at 25 °C</i> ^{18,19}			
Mass density	ρ_0	997.05	kg m ⁻³
Speed of sound	c_0	1496.7	m s ⁻¹
Compressibility	κ_0	447.7	TPa ⁻¹
Dynamic viscosity	η_0	0.890	mPa s
Bulk viscosity	η^b	2.485	mPa s
<i>Isotropic Pyrex borosilicate glass</i> ²⁰			
Mass density	ρ_{sl}	2230	kg m ⁻³
Elastic modulus	c_{11}	69.7	GPa
Elastic modulus	c_{44}	26.2	GPa
Mechanical damping coeff.	Γ_{sl}	0.0004	-
<i>Isotropic silver</i> ²¹			
Mass density	ρ_{sl}	10485	kg m ⁻³
Elastic modulus	c_{11}	133.9	GPa
Elastic modulus	c_{44}	25.9	GPa
Mechanical damping coeff.	Γ_{sl}	0.0004	-
<i>Cubic-symmetric silicon</i> ²²			
Mass density	ρ_{sl}	2329	kg m ⁻³
Elastic modulus	c_{11}	165.7	GPa
Elastic modulus	c_{44}	79.6	GPa
Elastic modulus	c_{12}	63.9	GPa
Mechanical damping coeff.	Γ_{sl}	0.0001	-
<i>Pz26 PZT ceramic</i> ^{23,24}			
Mass density	ρ_{sl}	7700	kg m ⁻³
Elastic modulus	c_{11}	168	GPa
Elastic modulus	c_{12}	110	GPa
Elastic modulus	c_{13}	99.9	GPa
Elastic modulus	c_{33}	123	GPa
Elastic modulus	c_{44}	30.1	GPa
Coupling constant	e_{15}	9.86	C/m ²
Coupling constant	e_{31}	-2.8	C/m ²
Coupling constant	e_{33}	14.7	C/m ²
Electric permittivity	ϵ_{11}	828	ϵ_0
Electric permittivity	ϵ_{33}	700	ϵ_0
Mechanical damping coeff.	Γ_{sl}	0.02	-

to the material, in this case glass (gl), and $c_{lo}^{(gl)}$ and $\lambda_{lo}^{(gl)}$ is the longitudinal sound speed and wavelength, respectively. The numerical error introduced by using the PML is shown in Fig. 3, in terms of the convergence parameter

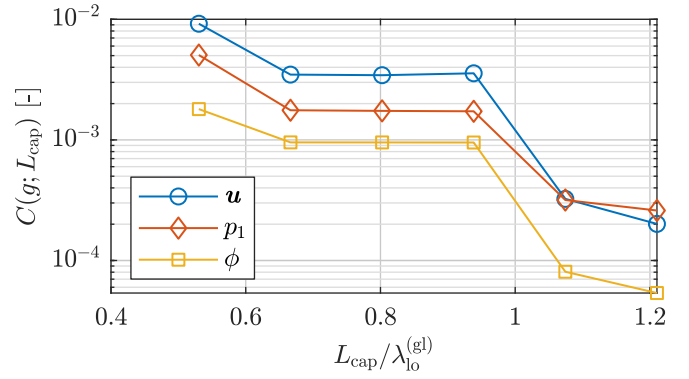


FIG. 3. Numerical convergence C for \mathbf{u} , p_1 , and φ in the PML of Fig. 2 at frequency $f_{res} = 3.84$ MHz with wavelength $\lambda_{lo}^{(gl)} = 1.47$ mm, PML length $L_{pml} = 413 \mu\text{m}$, and the physical system length L_{cap} is varied as $L_{cap}/\lambda_{lo}^{(gl)} = 0.53, 0.67, 0.80, 0.94, 1.07, \text{ and } 1.21$.

C , which for a given field solution g is defined by

$$C(g) = \sqrt{\frac{\int |g - g_{ref}|^2 dV}{\int |g_{ref}|^2 dV}}, \quad (9)$$

where g_{ref} is a reference solution. The integration domain is taken as the transducer region for $x \leq L_{pzt}/2$ defined in Fig. 2. In Fig. 3, the error measure C is evaluated at six different geometries at a fixed frequency $f = 3.84$ MHz with $\lambda_{lo}^{(gl)} = 1.47$ mm. The reference solution is taken as $L_{cap} = 1.35\lambda_{lo}^{(gl)}$. We choose the system length $L_{cap} = 1.07\lambda_{lo}^{(gl)}$ such that the maximal numerical error due to the unbounded PML is estimated to be $C = 3 \times 10^{-4}$.

B. Coupling-layer analysis in 3D and 1D

Continuing with the physics studies, we consider two coupling materials, a viscous mixture of 99 vol.% glycerol and 1 vol.% water, and a solid ED-20 epoxy resin, from now on referred to as glycerol and epoxy. The coupling material parameters used in the simulations are listed in Table IV.

In practice, the glycerol coupling allows for reusability of the acoustofluidic chip and/or the transducer, whereas the epoxy is used to ensure a well-defined but permanent coupling.^{8,25–28} The effect of the coupling layer is investigated by calculating the resonances as a function of coupling-layer material and thickness Δ using the 3D model. For each coupling-layer thickness Δ , the average acoustic energy density E_{ac} in the water-filled channel is computed as a function of frequency from 3.0 to 4.5 MHz. Resonances are then identified as peaks in the acoustic energy spectrum $E_{ac}(f)$. The resonances are illustrated in the scatter plot of Fig. 4, where the points represent resonances at frequency f for a coupling layer thickness Δ in the range from 0 to 100 μm , with point areas proportional to E_{ac}/E_{ac}^0 , where E_{ac}^0 is the acoustic energy density without a coupling layer. Also the res-

TABLE IV. List of the coupling layer parameters for glycerol (a 99% v/v glycerol and 1% v/v water mixture) and epoxy at 20 °C. The coefficient C_{12} of the epoxy is obtained through the relation $C_{12} = C_{11} - 2C_{44}$.

Parameter	Symbol	Value	Unit
<i>Glycerol</i> ^{29–31}			
Mass density	ρ_{glc}	1260.4	kg m^{-3}
Speed of sound	c_{glc}	1922.8	m s^{-1}
Compressibility	κ_{glc}	214.6	TPa^{-1}
Dynamic viscosity	η_{glc}	1.137	Pa s
Bulk viscosity	$\eta_{\text{glc}}^{\text{b}}$	0.790	Pa s
<i>Epoxy</i> ³²			
Mass density	ρ_{sl}	1205	kg m^{-3}
Elastic modulus	c_{11}	9.583	GPa
Elastic modulus	c_{44}	2.164	GPa
Mechanical damping coeff.	Γ_{sl}	0.01	-

onances of the unloaded PZT resonances are plotted to indicate where the transducer is most active.

The 3D model reveals a distinct behavior for both glycerol and epoxy coupling layers: As the coupling layer Δ increases, one resonance is attenuated (E_{ac} decreases) and has a large downshift in frequency, whereas another is sustained (E_{ac} increases) and has a small downshift in frequency. This behavior is also observed in an idealized 1D layer model along the vertical z -axis with seven domains: electrode, PZT, electrode, coupling layer, glass, water, glass of respective thicknesses H_{el} , H_{pzt} , H_{el} , Δ , $H_{\text{gl,bot}}$, H_{ch} , and $H_{\text{gl,top}}$. This 1D model takes into account only z -components, z -dependencies, densities and longitudinal sound speeds in the governing equations. The 1D model resonances are plotted together with the 3D resonances in Fig. 4. Of course, Fig. 4 reveals that the 3D model exhibits more resonances than the 1D model due to the extended degrees of freedom in the transverse directions and the shear waves. However, for the two indicated modes in each system, the 1D model agrees fairly well with the 3D model, which indicates that the attenuated and sustained resonance effect can be explained by this 1D fluid-like model.

C. A design criterion for coupling layers

The sustaining and attenuating behavior of the zero-layer resonances, as the layer thickness Δ is changed from 0 to 100 μm , is elucidated by studying the pressure profiles for each of the resonances in the 1D model. For each profile we choose a temporal phase factor $e^{-i\omega t}$ that gives the maximum *positive amplitude* in the PZT domain.

In Fig. 5(a) the 1D resonance pressure profiles are evaluated at three different epoxy coupling-layer thicknesses $\Delta = 0, 20,$ and $50 \mu\text{m}$ for the sustained resonance.

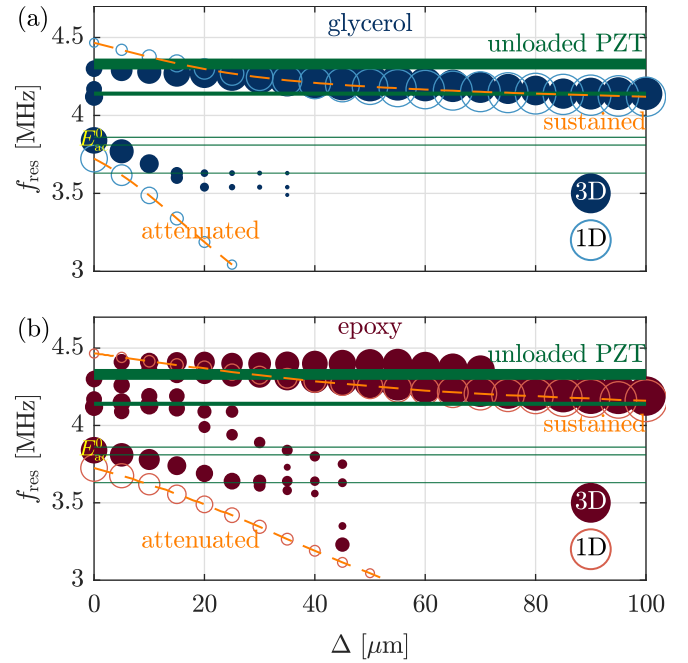


FIG. 4. Resonance frequencies in the capillary-tube device, as a function of increasing coupling-layer thickness Δ for (a) glycerol and (b) epoxy. The 3D and 1D model resonance frequencies are plotted as filled and empty circles, respectively, with an area proportional $E_{\text{ac}}/E_{\text{ac}}^0$. The dashed lines represent the 1D resonance frequencies, indicating a sustained or attenuated behavior. The solid green lines indicate unloaded PZT resonances with a linewidth proportional to the logarithm of the acoustic energy density in the PZT.

In Fig. 5(b), the same is shown for the attenuated resonance. Without the coupling layer, the fluid-solid interface is located at $z_0 = H_{\text{pzt}} + 2H_{\text{el}} + H_{\text{gl,bot}} = 558 \mu\text{m}$, and with a coupling layer at $z_{\Delta} = z_0 + \Delta$. As a result, the value of the pressure $p_1(z_{\Delta})$ is decreasing. In Fig. 5(a), labeled "sustained", we have $p_1(z_{\Delta}) < p_1(z_0) < 0$, yielding an *increased magnitude* of the pressure as Δ is increased. In contrast, in Fig. 5(b), labeled "attenuated", we have $0 < p_1(z_{\Delta}) < p_1(z_0)$, yielding a *decreasing magnitude* of the pressure for increasing Δ . Clearly, if a given zero-layer resonance has a negative (positive) value of $p_1(z_0)$ for the specified temporal phase factor, the resonance is sustained (attenuated). The sign of $p_1(z_0)$ is determined by the accumulated spatial phase factor $\Phi(z_0)$ of the fluid-solid value $p_1(z_0)$ relative to the surface value $p_1(0)$. In the 1D model, $\Phi(z_0)$ is given by the wavenumber k_i and layer thickness H_i of each layer ($i = \text{PZT, electrodes, and glass placed at } z < z_0$). Consequently, we arrive at the criterion,

$$\text{sustaining coupling if } \Phi(z_0) > \pi, \quad (10a)$$

$$\text{attenuating coupling if } \Phi(z_0) < \pi, \quad (10b)$$

$$\text{with } \Phi(z_0) = \sum_i k_i H_i = \sum_i \frac{\omega}{c_{\text{lo}}^{(i)}} H_i. \quad (10c)$$

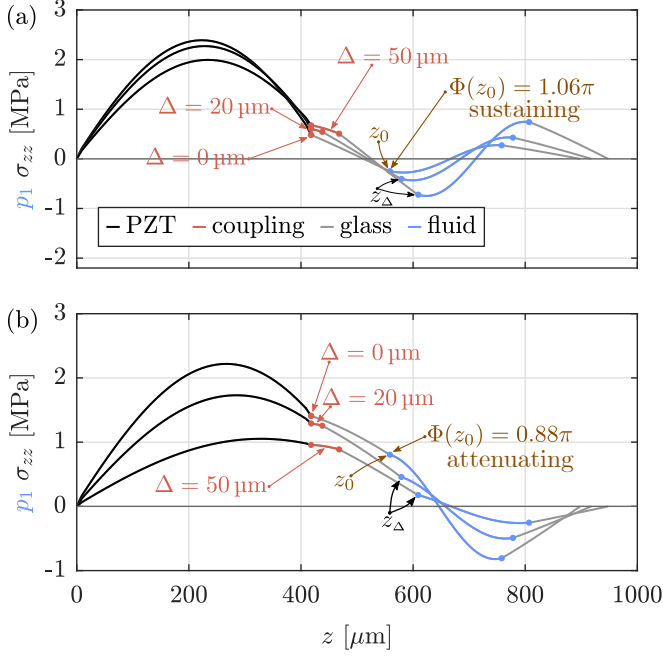


FIG. 5. Plots of normal stress $\sigma_{zz}(z)$ and pressure $p_1(z)$ in the 1D model with an epoxy coupling layer for the three layer thicknesses $\Delta = 0, 20,$ and $50 \mu\text{m}$ for (a) the sustained and (b) the attenuated zero-layer resonance modes. The profiles are plotted at a phase where the amplitude is at a maximum. The accumulated phase Φ is calculated without a coupling layer at the fluid-solid interface at $z_0 = H_{\text{pzt}} + 2H_{\text{el}} + H_{\text{gl,bot}}$ (brown arrow).

Note that this criterion is only valid for $|\Phi(z_0)| < \frac{3}{2}\pi$. For the given capillary-tube device, the values of $\Phi(z_0)$ for the sustained and the attenuated zero-layer resonance is $3.32 = 1.06\pi$ and $2.77 = 0.88\pi$, respectively. This criterion is one of the main results of the paper. It can be used to design optimally coupled capillary devices with minimum attenuation caused by the coupling layer.

D. Characteristic coupling-layer attenuation thickness Δ_0

Based on the 1D model, we derive a semi-analytical estimate for the characteristic thickness Δ_0 , at which the acoustic energy is attenuated for the above-mentioned attenuated zero-layer resonance modes, see Fig. 6. The pressure solution $p_{1,i}$ to the Helmholtz equation in each domain i , is written as

$$p_{1,i} = p_{a,i} \sin(k_i z + \phi_i) \quad \text{for } z \in \Omega_i. \quad (11)$$

At the interface between domain i and $i+1$, the acoustic pressure and velocity must be continuous,

$$p_{1,i+1} = p_{1,i}, \quad \frac{1}{\rho_{i+1}} \partial_z p_{1,i+1} = \frac{1}{\rho_i} \partial_z p_{1,i}. \quad (12)$$

This results in an iterative formula for the amplitude $p_{a,i}$ and phase ϕ_i with coefficients $\beta_{i+1,i}$, $a_{i+1,i}$, and $b_{i+1,i}$,

$$p_{a,i+1} = \beta_{i+1,i} p_{a,i}, \quad (13a)$$

$$\phi_{i+1} = \phi_i - k_{i+1} \sum_j^i H_j + \arctan(a_{i+1,i}/b_{i+1,i}), \quad (13b)$$

$$\beta_{i+1,i} = \sqrt{1 + \cos^2(k_i \sum_j^i H_j + \phi_i)(Z_{i+1,i}^2 - 1)}, \quad (13c)$$

$$a_{i+1,i} = \beta_{i+1,i}^{-1} \sin(k_i \sum_j^i H_j + \phi_i), \quad (13d)$$

$$b_{i+1,i} = \beta_{i+1,i}^{-1} Z_{i+1,i} \cos(k_i \sum_j^i H_j + \phi_i), \quad (13e)$$

$$Z_{i+1,i} = \frac{\rho_{i+1} c_{1o}^{(i+1)}}{\rho_i c_{1o}^{(i)}}. \quad (13f)$$

For a coupling layer (cl) made of either epoxy or glycerol, we have a mismatch $Z_{\text{cl,pzt}} \ll 1$ in the acoustic impedance, and the pressure amplitude $p_1(z_0)$ at the interface z_0 can therefore be approximated as

$$p_1(z_0) \approx p_0 \sqrt{\alpha^2 + \beta^2} \sin(k_{\text{cl}} H_{\text{pzt}}) \quad (14a)$$

$$\times \sin(\arctan(\alpha/\beta) + k_{\text{gl}} H_{\text{gl}}) + \mathcal{O}(Z_{\text{cl,pzt}}),$$

$$\text{with } \alpha = Z_{\text{gl,cl}} \sin(k_{\text{cl}} \Delta) \text{ and } \beta = \cos(k_{\text{cl}} \Delta). \quad (14b)$$

By further assuming $E_{\text{ac}} \propto p_1^2(z_0)$ and $k_{\text{cl}}^2 \Delta^2 \ll 1$, the lowest order functional dependence in the layer-thickness Δ becomes

$$E_{\text{ac}} \propto p_0^2 \sin^2(k_{\text{cl}} H_{\text{pzt}}) \quad (15)$$

$$\times \left[\cos^2(k_{\text{gl}} H_{\text{gl}}) - Z_{\text{gl,cl}} k_{\text{cl}} \Delta \sin(2k_{\text{gl}} H_{\text{gl}}) \right].$$

By setting $E_{\text{ac}} = 0$, we extract the characteristic thickness scale Δ_0 , at which the resonance is attenuated

$$\Delta_0 = \frac{Z_{\text{cl,gl}} c_{1o}^{(\text{cl})}}{2\omega} \cot\left(\frac{\omega H_{\text{gl}}}{c_{1o}^{(\text{gl})}}\right). \quad (16)$$

In Fig. 6 the normalized acoustic energy density $E_{\text{ac}}(\Delta)/E_{\text{ac}}^0$ is plotted as a function of the normalized

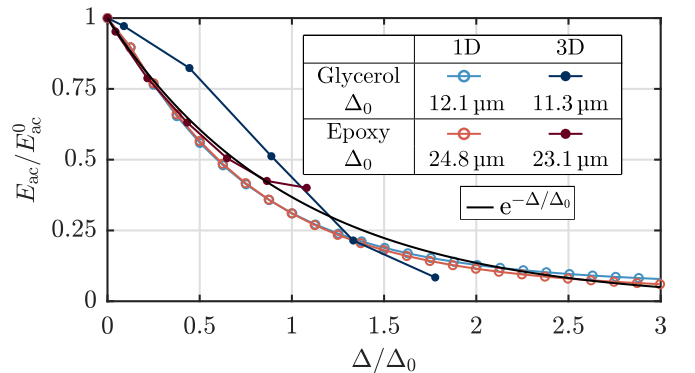


FIG. 6. The normalized acoustic energy density $E_{\text{ac}}/E_{\text{ac}}^0$ for the attenuated capillary-tube resonance versus the normalized coupling-layer thickness Δ/Δ_0 for glycerol and epoxy, simulated in the 3D and in the 1D model. The exponential function $e^{-\Delta/\Delta_0}$ (black) is inserted as a guide to the eye.

coupling-layer thickness Δ/Δ_0 . The acoustic energy is seen to be attenuated on the length scale Δ_0 predicted by Eq. (16), with $\Delta_0 = 12.1\ \mu\text{m}$ and $24.8\ \mu\text{m}$ for glycerol and epoxy, respectively. For both coupling materials, we observe an approximate exponential decay, $E_{ac}(\Delta)/E_{ac}^0 = e^{-\Delta/\Delta_0}$. The figure also show, that the attenuation computed in the 3D model is captured fairly well by the 1D model, including good quantitative agreement within 7% between the estimated characteristic length scale Δ_0 in 1D and 3D, respectively.

IV. ACOUSTOPHORETIC BULK DEVICES

We now move on to the second type of acoustofluidic devices, namely the bulk silicon-glass devices used in many lab-on-a-chip applications, as reviewed by Lenshof, Magnusson and Laurell.³³ As sketched in Fig. 1(b), these devices consist of a silicon-glass-based acoustofluidic chip coupled to a bulk PZT transducer. In contrast to the capillary-tube devices, the manipulation of particles in the silicon-glass chip relies on horizontal half-wave pressure resonances. Because the pressure half-wave is anti-symmetric around the vertical center plane of the channel, the symmetric motion actuated by a usual PZT transducer must be broken. This is normally done geometrically, by placing the transducer off-center,^{8,14,34} or by splitting the top electrode of the transducer, and actuate it by an anti-symmetric voltage actuation.^{28,35} In this work we use the former method, and displace the silicon-glass chip by $y_0 = 1\ \text{mm}$ with respect to the (xz) -mirror-plane of the PZT transducer, see Fig. 7.

A. Coupling layer analysis in 2D

It is well known that even with an ideal long straight channel in such devices, axial variations and acoustic hot spots appears along the channel.³⁶ However, when studying a region in the channel near a local maximum in the acoustic field, where the axial gradients are vanishing small, 2D models describes the acoustic fields very well.^{14,36} In this analysis, we therefore study the silicon-glass device in a 2D model as shown in Fig. 7. As introduced in Section II, the PZT transducer is a z -polarized Meggitt-Pz26 transducer, but now with a thickness of $1000\ \mu\text{m}$ with a resonance mode near 2 MHz. The materials and dimensions used in the silicon-glass-device simulations are listed in Tables III and V, respectively.

The coupling layer analysis is analogous to the one in Section III. The acoustic resonances are located as peaks in the acoustic energy density spectrum $E_{ac}(f)$ in the frequency range 1.5 to 2.5 MHz as a function of coupling material (glycerol or epoxy) and layer thickness Δ from 0 to $100\ \mu\text{m}$.

Similar to Fig. 4, we show in Fig. 8(a) a scatter plot, where the points represent resonances at frequency f for a coupling layer thickness Δ in the range from 0 to $100\ \mu\text{m}$, with point areas proportional to E_{ac}/E_{ac}^0 . Multiple resonances are identified, however, the one at $f_{res} = 1.940\ \text{MHz}$ stands out with E_{ac}^0 being more than

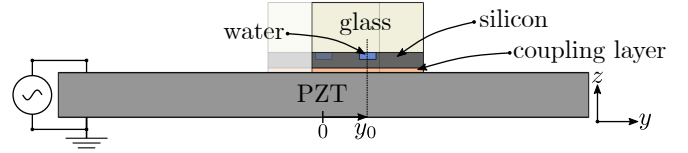


FIG. 7. Cross-section in the vertical yz -plane of the silicon-glass device in Fig. 1(b) showing the PZT transducer, the coupling layer, and the silicon-glass chip with the microchannel. The chip is displaced from the PZT center plane by $y_0 = 1\ \text{mm}$. The sketch defines the 2D model.

TABLE V. The width (W) and height (H) of the silicon (si), the glass cover (gl), the channel (ch), the piezoelectric transducer (pzt), and the silver electrodes (el).

Symbol	Value	Symbol	Value
W_{si}	$2520\ \mu\text{m}$	H_{si}	$350\ \mu\text{m}$
W_{gl}	$2520\ \mu\text{m}$	H_{gl}	$1130\ \mu\text{m}$
W_{ch}	$377\ \mu\text{m}$	H_{ch}	$157\ \mu\text{m}$
W_{pzt}	$12000\ \mu\text{m}$	H_{pzt}	$982\ \mu\text{m}$
W_{el}	$12000\ \mu\text{m}$	H_{el}	$9\ \mu\text{m}$

60 times larger than any other zero-layer peak. The frequency of this resonance is nearly independent of the coupling material and the layer thickness Δ . However, in Fig. 8(b) we see a fundamental difference between the two coupling materials: for glycerol the normalized acoustic energy density E_{ac}/E_{ac}^0 decreases rapidly to nearly zero at a length scale $\sim 100\ \text{nm}$, whereas for epoxy E_{ac}/E_{ac}^0 stays nearly constant up to $\Delta \sim 1\ \mu\text{m}$ followed by a slow drop to 0.75 at $\Delta = 10\ \mu\text{m}$ and 0.2 at $\Delta \sim 50\ \mu\text{m}$. This behavior may be explained by the geometry of the acoustics and the fundamental mechanical difference between elastic solids and viscous fluids. In the silicon-glass device, the direction of the standing pressure half-wave is orthogonal to the transducer polarization, and to excite this resonance mode, the transmission of shear-waves from the transducer to the microchannel is required. However, only a solid coupling layer, and not a viscous fluid, can support such transmission of shear waves.

B. Dissipation in the glycerol coupling layer

The critical glycerol coupling-layer thickness $\Delta_{crit} = 100\ \text{nm}$ observed in Fig. 8(c) requires a physical explanation, as this length scales is far from any of the geometrical sizes or acoustic wavelengths in the system. The small thickness $\Delta < 0.1\ \text{mm}$ of the coupling layer implies large shear strain rates, and a large amount of viscous dissipation. We assume that Δ_{crit} is the coupling-layer thickness where the time-averaged viscous dissipation power

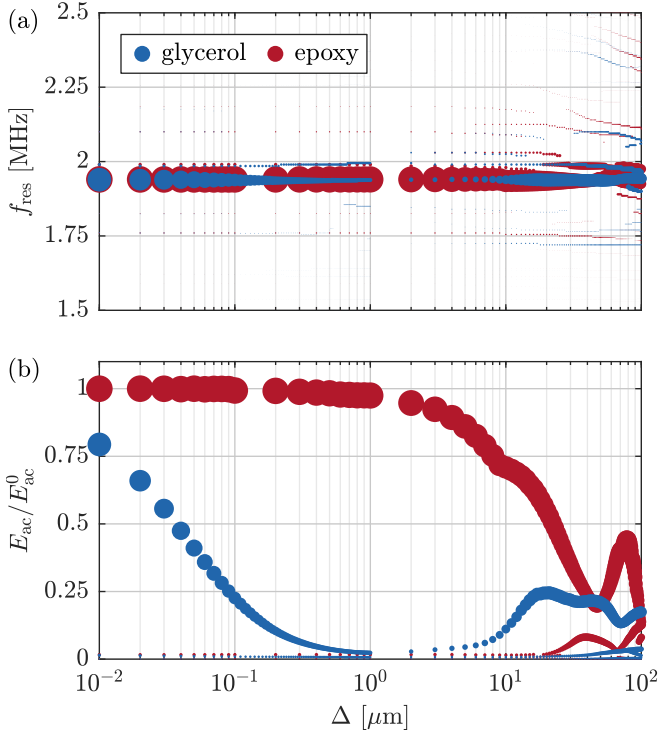


FIG. 8. Scatter plots with point areas proportional to E_{ac}/E_{ac}^0 of responses to increasing coupling-layer thickness Δ simulated in the 2D model of the silicon-glass device. (a) Resonance frequencies f_{res} . (b) Normalized acoustic energy density E_{ac}/E_{ac}^0 .

$\langle P_{crit}^{visc} \rangle$ in the glycerol coupling layer equals the time-averaged acoustic power $\langle P_{ac} \rangle$ delivered to the half-wave pressure resonator. For an ideal resonator with height H_{ch} , average acoustic energy density E_{ac} , and quality factor Q , together with a coupling layer of thickness Δ_{crit} , width W_{glc} , and dynamic viscosity η_{glc} , we obtain

$$\langle P_{ac} \rangle = \langle P_{crit}^{visc} \rangle, \quad (17a)$$

$$\langle P_{ac} \rangle = \int \langle p_1 \mathbf{v}_1 \cdot \mathbf{n} \rangle dA = \frac{16\pi}{Q} c_0 E_{ac} H_{ch}, \quad (17b)$$

$$\langle P_{crit}^{visc} \rangle = \int \langle \nabla \mathbf{v}_1 : \boldsymbol{\tau} \rangle dV \approx \frac{4\pi^2 \eta_{glc} E_{ac}}{Q^2 \rho_0 \Delta_{crit}} W_{glc}. \quad (17c)$$

Solving for Δ_{crit} , we obtain

$$\Delta_{crit} = \frac{\pi \eta_{glc} W_{glc}}{4Q \rho_0 c_0 H_{ch}}. \quad (18)$$

The effect of the surrounding silicon-glass chip is included in the quality factor $Q = f_{res}/\Delta f$, found from the resulting full-width Δf at half maximum of the corresponding resonance peak $E_{ac}(f)$ at the resonance frequency f_{res} . The estimate for Δ_{crit} is validated numerically by varying the material and geometrical parameters in (18). The chosen material and geometric variations are listed

TABLE VI. Critical coupling-layer thickness Δ_{crit} and quality factor Q in nine different system configurations, categorized as material and geometry variations.

Parameter	Material							Geometry	
	$0.05\eta_{glc}$	$0.1\eta_{glc}$	$0.2\eta_{glc}$	$0.5\eta_{glc}$	η_{glc}	$2\eta_{glc}$	$2\rho_0$	$0.5H_{ch}$	$0.5W_{glc}$
Δ_{crit} [nm]	3.4	6.9	13.7	34.3	68.5	137.0	73.0	202.2	38.5
Q [-]	140	140	140	140	140	140	140	95	125

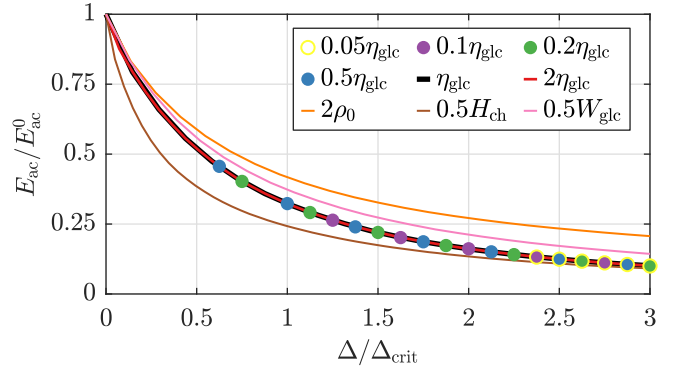


FIG. 9. Simulated normalized acoustic energy density E_{ac}/E_{ac}^0 versus the normalized coupling layer thickness Δ/Δ_{crit} for the nine different system configurations listed in Table VI.

in Table VI together with critical thicknesses and quality factors. Using the 2D model, the acoustic energy density E_{ac} is simulated, and the result is normalized by E_{ac}^0 , the value without a coupling layer. In Fig. 9 the simulated E_{ac}/E_{ac}^0 is plotted versus the normalized coupling-layer thickness Δ/Δ_{crit} , and for the wide range of parameters, it is seen that indeed E_{ac}/E_{ac}^0 decays on the critical coupling-layer thickness scale Δ_{crit} .

V. CONCLUSION

We have developed a numerical 3D model to study the role of coupling layers in acoustofluidic devices. The model includes the PZT transducer with electrodes, the coupling layer, and the acoustofluidic chip with the fluid-filled microchannel. The model is used to study two well-known types of acoustofluidic devices: a glass capillary tube and a silicon-glass chip, classified as vertical and horizontal resonators, respectively, relative to the polarization axis of the transducer. For each device, a viscous glycerol and a solid epoxy coupling layer was studied.

For vertical resonators, the capillary-tube device, we have found that for a given zero-layer resonance, the coupling layer can either result in a sustaining or attenuating resonance. We have established the criterion (10) to predict which of the two behaviors will occur, based on a relation involving the phase of the acoustic wave. For the attenuated waves, we have derived expression (16) to

estimate the characteristic layer thickness Δ_0 at which the resonance is attenuated.

For horizontal resonators, the silicon-glass device, the acoustic resonances are partially powered by shear-wave transmission through the coupling layer. Since a fluid cannot sustain such a shear, the glycerol coupling layer works as a dissipative layer. A critical viscous dissipation thickness Δ_{crit} was presented in Eq. (18), based on scaling arguments in a 1D two-component model.

The simulation results presented, has led to the formulation of design rules for choosing an optimal coupling layer between the piezoelectric transducer and the acoustofluidic device. The design rules involves material parameters, geometrical parameters, and information about the orientation of the given acoustic resonance mode relative to the polarization axis of the transducer. We hope that these rules will prove useful, and that their limitations will be understood better by experimental validation.

ACKNOWLEDGMENTS

The authors were supported by Independent Research Fund Denmark, Technology and Production Sciences (Grant No. 8022-00285B).

- ¹V. T. Rathod, “A review of acoustic impedance matching techniques for piezoelectric sensors and transducers,” *Sensors* **20**(14), 4051 (2020) doi: [10.3390/s20144051](https://doi.org/10.3390/s20144051).
- ²M. Hill, Y. Shen, and J. J. Hawkes, “Modelling of layered resonators for ultrasonic separation,” *Ultrasonics* **40**(1-8), 385–392 (2002) doi: [10.1016/S0041-624X\(02\)00127-0](https://doi.org/10.1016/S0041-624X(02)00127-0).
- ³P. Glynne-Jones, R. J. Boltryk, and M. Hill, “Acoustofluidics 9: Modelling and applications of planar resonant devices for acoustic particle manipulation,” *Lab Chip* **12**(8), 1417–1426 (2012) doi: [10.1039/c2lc21257a](https://doi.org/10.1039/c2lc21257a).
- ⁴B. Hammarström, T. Laurell, and J. Nilsson, “Seed particle enabled acoustic trapping of bacteria and nanoparticles in continuous flow systems,” *Lab Chip* **12**, 4296–4304 (2012) doi: [10.1039/C2LC40697G](https://doi.org/10.1039/C2LC40697G).
- ⁵J. Lei, P. Glynne-Jones, and M. Hill, “Acoustic streaming in the transducer plane in ultrasonic particle manipulation devices,” *Lab Chip* **13**(11), 2133–2143 (2013) doi: [10.1039/c3lc00010a](https://doi.org/10.1039/c3lc00010a).
- ⁶P. Mishra, M. Hill, and P. Glynne-Jones, “Deformation of red blood cells using acoustic radiation forces,” *Biomicrofluidics* **8**(3), 034109 (2014) doi: [10.1063/1.4882777](https://doi.org/10.1063/1.4882777).
- ⁷I. Gralinski, S. Raymond, T. Alan, and A. Neild, “Continuous flow ultrasonic particle trapping in a glass capillary,” *Journal of Applied Physics* **115**(5), 054505 (2014) doi: [10.1063/1.4863645](https://doi.org/10.1063/1.4863645).
- ⁸R. Barnkob, P. Augustsson, T. Laurell, and H. Bruus, “Measuring the local pressure amplitude in microchannel acoustophoresis,” *Lab Chip* **10**(5), 563–570 (2010) doi: [10.1039/b920376a](https://doi.org/10.1039/b920376a).
- ⁹C. Magnusson, P. Augustsson, A. Lenshof, Y. Ceder, T. Laurell, and H. Lilja, “Clinical-scale cell-surface-marker independent acoustic microfluidic enrichment of tumor cells from blood,” *Anal. Chem.* **89**(22), 11954–11961 (2017) doi: [10.1021/acs.analchem.7b01458](https://doi.org/10.1021/acs.analchem.7b01458).
- ¹⁰K. Petersson, O. Jakobsson, P. Ohlsson, P. Augustsson, S. Scheduling, J. Malm, and T. Laurell, “Acoustofluidic hematocrit determination,” *Anal. Chim. Acta* **1000**, 199–204 (2018) doi: [10.1016/j.aca.2017.11.037](https://doi.org/10.1016/j.aca.2017.11.037).
- ¹¹N. R. Skov, J. S. Bach, B. G. Winkelmann, and H. Bruus, “3D modeling of acoustofluidics in a liquid-filled cavity including streaming, viscous boundary layers, surrounding solids, and a piezoelectric transducer,” *AIMS Mathematics* **4**, 99–111 (2019) doi: [10.3934/Math.2019.1.99](https://doi.org/10.3934/Math.2019.1.99).
- ¹²J. S. Bach and H. Bruus, “Theory of pressure acoustics with viscous boundary layers and streaming in curved elastic cavities,” *J. Acoust. Soc. Am.* **144**, 766–784 (2018) doi: [10.1121/1.5049579](https://doi.org/10.1121/1.5049579).
- ¹³P. B. Muller, R. Barnkob, M. J. H. Jensen, and H. Bruus, “A numerical study of microparticle acoustophoresis driven by acoustic radiation forces and streaming-induced drag forces,” *Lab Chip* **12**, 4617–4627 (2012) doi: [10.1039/C2LC40612H](https://doi.org/10.1039/C2LC40612H).
- ¹⁴P. B. Muller, M. Rossi, A. G. Marin, R. Barnkob, P. Augustsson, T. Laurell, C. J. Kähler, and H. Bruus, “Ultrasound-induced acoustophoretic motion of microparticles in three dimensions,” *Phys. Rev. E* **88**(2), 023006 (2013) doi: [10.1103/PhysRevE.88.023006](https://doi.org/10.1103/PhysRevE.88.023006).
- ¹⁵A. Bermúdez, L. Hervella-Nieto, A. Prieto, and R. Rodríguez, “An optimal perfectly matched layer with unbounded absorbing function for time-harmonic acoustic scattering problems,” *Journal of Computational Physics* **223**(2), 469–488 (2007) doi: [10.1016/j.jcp.2006.09.018](https://doi.org/10.1016/j.jcp.2006.09.018).
- ¹⁶COMSOL Multiphysics 5.5 (2019), <http://www.comsol.com>.
- ¹⁷M. W. H. Ley and H. Bruus, “Three-dimensional numerical modeling of acoustic trapping in glass capillaries,” *Phys. Rev. Applied* **8**, 024020 (2017) doi: [10.1103/PhysRevApplied.8.024020](https://doi.org/10.1103/PhysRevApplied.8.024020).
- ¹⁸P. B. Muller and H. Bruus, “Numerical study of thermoviscous effects in ultrasound-induced acoustic streaming in microchannels,” *Phys. Rev. E* **90**(4), 043016 (2014) doi: [10.1103/PhysRevE.90.043016](https://doi.org/10.1103/PhysRevE.90.043016).
- ¹⁹J. T. Karlsen, P. Augustsson, and H. Bruus, “Acoustic force density acting on inhomogeneous fluids in acoustic fields,” *Phys. Rev. Lett.* **117**, 114504 (2016) doi: [10.1103/PhysRevLett.117.114504](https://doi.org/10.1103/PhysRevLett.117.114504).
- ²⁰CORNING, Houghton Park C-8, Corning, NY 14831, USA, *Glass Silicon Constraint Substrates*, <http://www.valleydesign.com/Datasheets/Corning%20Pyrex%207740.pdf>, accessed 28 November 2019.
- ²¹AZoMaterials, Charlotte Street, Manchester, UK, *Silver - Applications and Properties of Silver*, <https://www.azom.com/properties.aspx?ArticleID=600>, accessed 27 November 2021.
- ²²M. A. Hopcroft, W. D. Nix, and T. W. Kenny, “What is the Young’s modulus of silicon,” *J. Microelectromech. Syst.* **19**, 229–238 (2010) doi: [10.1109/JMEMS.2009.2039697](https://doi.org/10.1109/JMEMS.2009.2039697).
- ²³Meggitt A/S, Porthusvej 4, DK-3490 Kvistgaard, Denmark, *Ferroperm Matdat 2017*, <https://www.meggittferroperm.com/materials/>, accessed 28 Januar 2021.
- ²⁴P. Hahn and J. Dual, “A numerically efficient damping model for acoustic resonances in microfluidic cavities,” *Physics of Fluids* **27**, 062005 (2015) doi: [10.1063/1.4922986](https://doi.org/10.1063/1.4922986).
- ²⁵J. J. Hawkes and W. T. Coakley, “Force field particle filter, combining ultrasound standing waves and laminar flow,” *Sensor Actuat B-Chem* **75**(3), 213–222 (2001) doi: [10.1016/S0925-4005\(01\)00553-6](https://doi.org/10.1016/S0925-4005(01)00553-6).
- ²⁶B. Hammarström, M. Evander, H. Barbeau, M. Bruzelius, J. Larsson, T. Laurell, and J. Nilsson, “Non-contact acoustic cell trapping in disposable glass capillaries,” *Lab Chip* **10**(17), 2251–2257 (2010) doi: [10.1039/c004504g](https://doi.org/10.1039/c004504g).
- ²⁷P. Ohlsson, M. Evander, K. Petersson, L. Mellhammar, A. Lehmusvuori, U. Karhunen, M. Soikkeli, T. Seppä, E. Tuunainen, A. Spangar, P. von Lode, K. Rantakokko-Jalava, G. Otto, S. Scheduling, T. Soukka, S. Wittfooth, and T. Laurell, “Integrated acoustic separation, enrichment, and microchip polymerase chain reaction detection of bacteria from blood for rapid sepsis diagnostics,” *Analytical Chemistry* **88**(19), 9403–9411 (2016) doi: [10.1021/acs.analchem.6b00323](https://doi.org/10.1021/acs.analchem.6b00323).
- ²⁸W. N. Bodé, L. Jiang, T. Laurell, and H. Bruus, “Microparticle acoustophoresis in aluminum-based acoustofluidic devices with

- PDMS covers,” *Micromachines* **11**(3), 292 (2020) doi: [10.3390/mi11030292](https://doi.org/10.3390/mi11030292).
- ²⁹W. Slie, A. Donfor Jr, and T. Litovitz, “Ultrasonic shear and longitudinal measurements in aqueous glycerol,” *The Journal of Chemical Physics* **44**(10), 3712–3718 (1966).
- ³⁰L. Negadi, B. Feddal-Benabed, I. Bahadur, J. Saab, M. Zaoui-Djelloul-Daouadji, D. Ramjugernath, and A. Negadi, “Effect of temperature on density, sound velocity, and their derived properties for the binary systems glycerol with water or alcohols,” *The Journal of Chemical Thermodynamics* **109**, 124–136 (2017) doi: [10.1016/j.jct.2017.01.011](https://doi.org/10.1016/j.jct.2017.01.011).
- ³¹N.-S. Cheng, “Formula for the viscosity of a glycerol-water mixture,” *Ind. Eng. Chem. Res.* **47**(9), 3285–3288 (2008) doi: [10.1021/ie071349z](https://doi.org/10.1021/ie071349z).
- ³²I. I. Perepechko, V. A. Danilov, and V. V. Nizhegorodov, “Ultrasonic velocity in epoxy resin at temperatures down to 4.2 K,” *Mechanics of Composite Materials* **32**, 316–320 (1996) doi: [10.1007/BF02254743](https://doi.org/10.1007/BF02254743).
- ³³A. Lenshof, C. Magnusson, and T. Laurell, “Acoustofluidics 8: Applications in acoustophoresis in continuous flow microsystems,” *Lab Chip* **12**, 1210–1223 (2012) doi: [10.1039/c2lc21256k](https://doi.org/10.1039/c2lc21256k).
- ³⁴A. Tahmasebipour, L. Friedrich, M. Begley, H. Bruus, and C. Meinhart, “Toward optimal acoustophoretic microparticle manipulation by exploiting asymmetry,” *J. Acoust. Soc. Am.* **148**(1), 359–373 (2020) doi: [10.1121/10.0001634](https://doi.org/10.1121/10.0001634).
- ³⁵R. P. Moiseyenko and H. Bruus, “Whole-system ultrasound resonances as the basis for acoustophoresis in all-polymer microfluidic devices,” *Phys. Rev. Applied* **11**, 014014 (2019) doi: [10.1103/PhysRevApplied.11.014014](https://doi.org/10.1103/PhysRevApplied.11.014014).
- ³⁶P. Augustsson, R. Barnkob, S. T. Wereley, H. Bruus, and T. Laurell, “Automated and temperature-controlled micro-PIV measurements enabling long-term-stable microchannel acoustophoresis characterization,” *Lab Chip* **11**(24), 4152–4164 (2011) doi: [10.1039/c1lc20637k](https://doi.org/10.1039/c1lc20637k).